

# ESI-GAL: EEG Source Imaging-based Kinematics Parameter Estimation for Grasp and Lift Task

Anant Jain and Lalan Kumar

**Abstract**—Electroencephalogram (EEG) signals-based motor kinematics prediction (MKP) has been an active area of research to develop brain-computer interface (BCI) systems such as exosuits, prostheses, and rehabilitation devices. However, EEG source imaging (ESI) based kinematics prediction is sparsely explored in the literature. In this study, pre-movement EEG features are utilized to predict three-dimensional (3D) hand kinematics for the grasp-and-lift motor task. A public dataset, WAY-EEG-GAL, is utilized for MKP analysis. In particular, sensor-domain (EEG data) and source-domain (ESI data) based features from the frontoparietal region are explored for MKP. Deep learning-based models are explored to achieve efficient kinematics decoding. Various time-lagged and window sizes are analyzed for hand kinematics prediction. Subsequently, intra-subject and inter-subject MKP analysis is performed to investigate the subject-specific and subject-independent motor-learning capabilities of the neural decoders. The Pearson correlation coefficient (PCC) is used as the performance metric for kinematics trajectory decoding. The rEEGNet neural decoder achieved the best performance with sensor-domain and source-domain features with a time lag and window size of 100 *ms* and 450 *ms*, respectively. The highest mean PCC values of 0.790, 0.795, and 0.637 are achieved using sensor-domain features, while 0.769, 0.777, and 0.647 are achieved using source-domain features in x, y, and z-directions, respectively. This study explores the feasibility of trajectory prediction using EEG sensor-domain and source-domain EEG features for the grasp-and-lift task. Furthermore, inter-subject trajectory estimation is performed using the proposed deep learning decoder with EEG source domain features.

**Index Terms**—Brain computer interface (BCI), electroencephalography, Deep learning, Motor kinematics prediction (MKP), inter-subject decoding, EEG, source imaging, sLORETA

## I. INTRODUCTION

### A. Background

Brain-computer interface (BCI), also known as brain-machine interfaces (BMIs), represent a cutting-edge technology that facilitates control over external devices through brain activity, bypassing the need for peripheral nerves and muscles [1]. This technology holds significant promise for enhancing the life quality of individuals with motor disabilities [2]–[7] and enables interaction with healthy individuals [8]–[10]. Over time, advancements in computational power and machine learning algorithms have empowered BCI systems to decode neural signals for

assisting, augmenting, or restoring motor functionality [11]. BCI systems encompass a series of sequential procedures comprising the acquisition and processing of neural signals, relevant feature extraction, intention detection, and user feedback signals generation. Invasive and non-invasive recording techniques are utilized for capturing neural activity. While invasive approaches offer greater accuracy in brain activity recognition, they necessitate surgical implantation of sensors beneath the scalp [12], [13]. Conversely, non-invasive BCIs capture neural signals by pacing sensors on the scalp. Various non-invasive techniques include functional near-infrared spectroscopy (fNIRS) [14], magnetoencephalography (MEG) [15], functional magnetic resonance imaging (fMRI) [16] and electroencephalogram (EEG) [17].

EEG-based BCI systems have gained popularity among these methods due to their high temporal resolution, portability, and cost-effectiveness. They have been utilized across various applications, such as fatigue and drowsiness detection [18], [19], emotion recognition [20], [21], wearable exoskeletons [22], [23], and robotic control [24]–[27]. Additionally, EEG-based BCIs have been employed for classifying motor imagery or motor execution tasks [28]–[31]. Although classification-based approaches have been extensively explored, continuous kinematic estimation-based approaches offer enhanced performance and efficient control of external devices such as neural prostheses, exosuits, or exoskeletons.

### B. Related work

EEG-based kinematics decoding has been performed in both motor execution task [32]–[34] and motor imagery task [35]. EEG-based kinematics decoding is performed for 2D center-out reaching task in [36] using multiple linear regression (mLR) decoder. EEG slow cortical potentials based upper limb trajectories (hand, elbow, and shoulder) decoding is reported in [37] using mLR decoding model. Hand kinematics decoding for unimanual target-reaching movement is investigated in [38] with Kalman filter (KF) and mLR decoders using scalp EEG signals. Recent studies have utilized deep learning-based decoders [39]–[44] for motor kinematics prediction (MKP) using scalp EEG signals. Knee joint angle trajectory is estimated using EEG signals with the NARX neural network in [39]. EEG-based MKP is investigated in [40] using a convolutional neural network - bidirectional long short-term memory (CNN-biLSTM) decoding model during unimanual target-reaching movement for controlling a robotic arm. MKP is performed for the grasp-and-lift task using a wavelet packet decomposition (WPD) based CNN-LSTM decoder in [42]. Low-frequency EEG signals are utilized in [41] for MKP with CNN-LSTM

Anant Jain is with the Department of Electrical Engineering, Indian Institute of Technology Delhi, New Delhi 110016, India (e-mail: anant-jain@ee.iitd.ac.in).

Lalan Kumar is with the Department of Electrical Engineering, Bharti School of Telecommunication, and Yardi School of Artificial Intelligence, Indian Institute of Technology Delhi, New Delhi 110016, India (e-mail: lkumar@ee.iitd.ac.in).

decoding architecture. The inter-subject decoding analysis is investigated in [43] using EEG signals along with deep learning-based decoding models. Elbow joint angle trajectory decoding is performed in [44] using an attention-based CNN-LSTM decoder with EEG signals during the biceps-curl task.

In the field of brain-computer interface (BCI) research, non-invasive investigations have traditionally focused on utilizing EEG signals directly, operating within the sensor space. However, advancements in EEG source imaging (ESI) techniques enable the inference of cortical sources from non-invasive brain signals. This approach has prompted studies exploring decoding brain activity in the source space via ESI. The application of source-space decoding has predominantly been investigated within the classification domain, encompassing tasks such as motor imagery classification [45]–[47], arm direction classification [48] and gesture (alphabets) recognition [49]. Across these studies, source-space classification has frequently demonstrated enhanced performance compared to traditional sensor space methods. ESI-based MKP has been explored for reach-to-target task [50], snake trajectory tracking [51] and grasp-and-lift task [52]. In [50], the mLR decoder is deployed to estimate hand, elbow, and shoulder trajectories during a target-reaching experiment utilizing EEG current source dipoles. The study reported an average correlation of  $0.36 \pm 0.13$  across all trajectories for actual movement execution. Source-space EEG-based hand trajectory estimation is conducted by employing a combination of the partial least squares (PLS) regression model and the square-root unscented Kalman filter (SR-UKF) in [51]. The study reported the highest average correlation of  $0.31 \pm 0.09$  and  $0.35 \pm 0.09$  for hand position and velocity, respectively. In [52], hand trajectory estimation is performed for the grasp-and-lift task using EEG source-domain signals with a residual CNN-LSTM neural decoder. The mean Pearson correlation coefficient of 0.59, 0.61, and 0.56 is reported for the window size of 300 ms in the x, y, and z directions, respectively.

### C. Objectives and Contribution

In this study, MKP is performed using sensor-domain and source-domain EEG features for the grasp-and-lift task. Pre-movement EEG segments are utilized for kinematics estimation along with convolutional neural network (CNN) based deep learning models for external device (exosuit, prosthesis) control-based BCI applications. The open-source WAY-EEG-GAL [53] database is used for the proposed methodology. The sensor-domain and source-domain features are explored for motor kinematics prediction during the grasp-and-lift task. The frontoparietal regions are utilized as regions of interest (ROI) for both sensor-domain and source-domain-based feature selection. Additionally, inter-subject decoding performance is evaluated to demonstrate the subject-adaptability of the proposed kinematics decoding framework.

The organization of the article is as follows: Section II includes the dataset description (Section II-A), data preprocessing (Section II-B), EEG source Imaging and feature extraction (Section II-C), deep-learning models (Section II-D), and experimental details (Section II-E). Performance evaluation for

MKP and an extensive discussion of the results are detailed in Section III and Section IV provides the conclusions about the research work.

## II. MATERIALS AND METHODS

This Section includes a detailed description of the experimental paradigm, dataset, data pre-processing pipeline, feature extraction, EEG source imaging, and neural decoders for trajectory estimation. An overview of the proposed trajectory estimation framework is shown in Fig. 1.

### A. Dataset Description

WAY-EEG-GAL (Wearable interfaces for hAnd function recovery EEG grasp and lift) dataset [53] is used for MKP. Synchronous EEG and hand kinematics data were collected during the grasp-and-lift task. EEG data was recorded using 32-channel active EEG electrodes (actiCAP, *Brain Products GmbH, Germany*) in conjunction with a biosignal amplifier (BrainAmp, *Brain Products GmbH, Germany*) at a 500 Hz sampling rate. The hand kinematics data was acquired using a 3D position sensor (FASTRAK, *Polhemus Inc., USA*) with a 500 Hz sampling frequency. In particular, the neural and kinematics data of twelve participants while performing the right-hand grasp-and-lift task is included in the dataset.

In each trial, participants were instructed to perform a grasp-and-lift task on an object. The task involved reaching for a small object, gripping it between the index finger and thumb, elevating it a few centimeters into the air, maintaining a stable hold briefly, and replacing and releasing it to its original position. The initiation of the reaching motion and the controlled lowering of the object were prompted by a visual cue in the form of an LED signal. The participants had autonomy over the overall pace of the task, allowing for a naturalistic execution. Throughout the experimental sessions, the object's properties underwent systematic variations in physical properties. These variations encompassed unpredictable changes in weight (165, 330, or 660 g) and the contact surface (sandpaper, suede, or silk).

### B. Data Preprocessing

Neural data preprocessing is performed using the open-source plugin EEGLAB [54] in the MATLAB software package. Initially, the raw EEG data is band-pass filtered using a zero-phase Hamming windowed sync FIR filter ranging between 0.1 and 40 Hz to eliminate artifacts in the low band (e.g., baseline drift and motion artifacts) and high band (e.g., electromyogram (EMG)). Subsequently, the filtered EEG data is re-referenced using common average referencing (CAR), followed by Independent Component Analysis (ICA) to eliminate artifacts related to electrooculography (EOG) and EMG. The number of removed independent components ranged from three to six across subjects, with the removed components primarily projecting over frontal cortical areas following the inverse ICA transform. Further, downsampling of denoised EEG data to 100 Hz sampling rate is performed for reduction of the computational cost. Eighteen EEG sensors around the motor-cortex region are selected for MKP.

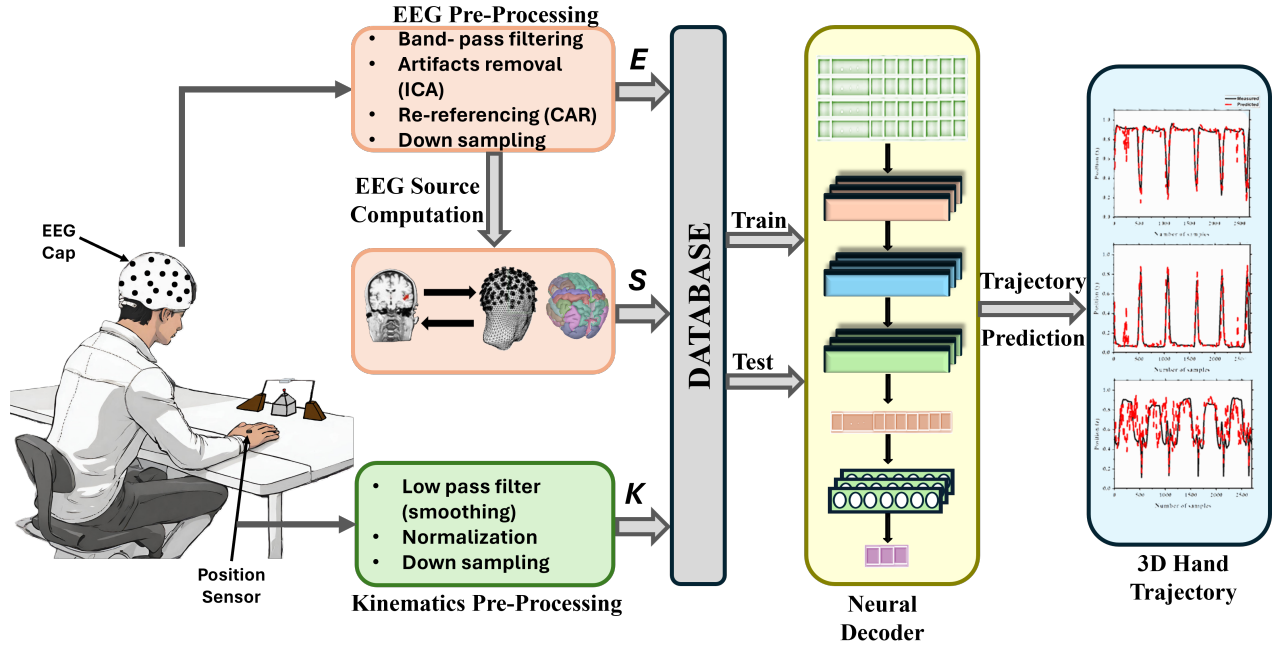


Fig. 1. Flowchart of proposed kinematics decoding framework for Grasp-and-Lift task.

Two key steps were involved in kinematic data preprocessing to eliminate measurement noise and signal scaling. First, a low-pass filter with a cutoff frequency of 2 Hz is applied to remove measurement noise from raw kinematics data. For scaling, min-max normalization is employed to scale the filtered data onto a range of  $[0, 1]$  as follows:

$$K[t] = \frac{k[t] - k_{min}}{k_{max} - k_{min}} \quad (1)$$

where,  $K[t]$  and  $k[t]$  are the normalized and measured position coordinate values, respectively.  $k_{max}$  and  $k_{min}$  are maximum and minimum hand position coordinates, respectively. For scaling the kinematics data in the range of  $[0, 1]$ , min-max normalization is performed for the  $x$ ,  $y$ , and  $z$  position coordinates. Further, the normalized kinematics data is downsampled from 500 Hz to 100 Hz sampling rate.

### C. EEG Source Imaging

As the neural electrical signals transmit from the cortical surface to the scalp, they undergo distortion and dispersion due to volume-conduction effects. EEG source imaging (ESI) has the potential to mitigate cross-electrode correlation that results due to volume conduction effects. The fundamental principle behind ESI involves the estimation of primary cortical current activations based on the recorded scalp EEG signals. Two primary stages are involved in ESI: the solution of the forward problem and the inverse problem. The solution for the forward problem employs an anatomical head model to define the mapping between the voltages detected by EEG sensors on the scalp and the current activations originating from the cortical surface sources. Subsequently, the solution to the inverse problem aims to identify the cortical current distribution that

aligns the scalp potential within a predefined set of constraints. It can be noted that scalp EEG data undergoes mapping onto a higher-dimensional cortical source grid with typical EEG sensors of around 30 and an estimated number of source dipoles of around 15,000. Due to the significant difference in the number of sensors and sources, ESI becomes a highly underdetermined problem. The two stages involved in the ESI are further detailed below:

1) *Forward Problem*: The computation of the lead field matrix is carried out in the forward modeling stage. The lead field matrix depicts the transmission of cortical source currents through various conductivity layers to the scalp electrodes. This procedure integrates the principles of EEG generation, incorporating considerations of Neumann and Dirichlet boundary conditions to establish the relationship between voltages recorded at the scalp and cortical current densities. The mathematical relationship can be expressed as:

$$[\mathbf{E}]_{I \times N_s} = [\mathbf{A}]_{I \times K} [\mathbf{S}]_{K \times N_s} + [\boldsymbol{\eta}]_{I \times N_s} \quad (1)$$

where,  $\mathbf{E}$  represents pre-processed scalp EEG data,  $I$  is the total number of EEG sensors ( $=32$ ),  $\mathbf{A}$  is the lead-field matrix,  $\mathbf{S}$  denotes source activity,  $\mathbf{K}$  is the total number of source dipoles, and  $\boldsymbol{\eta}$  is the measured noise.

The boundary element method (BEM) is utilized to compute the head model by employing the ICBM152 MRI template [55] as the anatomy and subsequently co-registering with the positions of the EEG electrodes. The forward modeling is performed using the OpenMEEG [56] with parameters  $\sigma_{scalp} = 1$ ,  $\sigma_{skull} = 0.0125$ , and  $\sigma_{brain} = 1$ . In particular, the Brainstorm toolbox [57] is utilized for EEG source imaging (ESI).

2) *Inverse Problem*: The objective for solving the ESI inverse problem is to estimate the cortical source current

signal  $[S]$  using the lead field matrix  $[A]$ , derived from the head model computation. A noise perturbation matrix  $[\eta]$  is introduced to account for errors resulting from solving the ill-posed and ill-conditioned inverse problem. In this study, the inverse problem is solved using the standard low-resolution electrical tomography (sLORETA) [58] method. sLORETA is utilized with normal to cortex dipole orientation and minimum norm imaging.

As a result of the transformation into source space, the number of signals increases to 15,000 source signals from 32 scalp EEG signals. The primary aim of regions of interest (ROI) scouting is to sub-group the number of signals within the source space based on different brain regions. The ROIs of the brain cortical area are defined based on the Mindboggle atlas [59] for the ICBM152 MRI template. There are a total of 62 ROIs defined for the Mindboggle atlas. However, even defined ROIs consist of signals in the order of hundreds. Hence, the mean of cortical source signals across each ROI for each timestamp is utilized. Further, ROIs are selected in the frontoparietal region of the brain. The selected ROIs are caudalmiddlefrontal (CMF), lateralorbitofrontal (LOF), medialorbitofrontal (MOFL), superiorfrontal (SF), paracentral (PCL), postcentral (PoCL), precentral (PreCL), superiorparietal (SP) and inferiorparietal (IP). In particular, a total of 15 ROIs were selected for the trajectory decoding, as shown in Fig. 2.

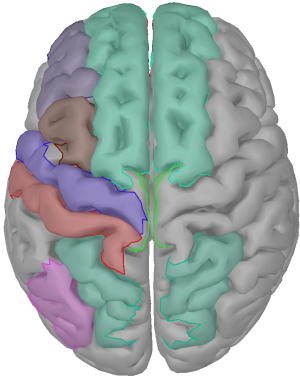


Fig. 2. Selected 15 Region of Interest (ROI) using Mindboggle Atlas

#### D. Decoding Models

Convolutional neural network (CNN) based Deep Learning architectures have achieved high accuracy for various EEG-based BCI applications. In this study, we have utilized modified versions of three popular architectures, EEGNet [60], DeepConvNet [61], and ShallowConvNet [61], for continuous trajectory estimation. The modified versions of the models are depicted as rEEGNET, rDeepConvNet, and rShallowConvNet, where 'r' is the abbreviation for 'regression' here. The model architectures are summarized in tables I to III; however, a comprehensive description is provided in the subsequent subsections:

1) *rEEGNet*: It is a CNN-based compact architecture employed across various BCI tasks. The compact nature of the decoder offers the advantage of efficient training with

limited data. This study uses a modified version of EEGNet architecture for trajectory estimation. The model architecture can be segmented into two stages. In the first stage, a 2D convolutional (Conv) layer comprising 32 filters with kernel size (1, 32) is applied to the input signals. Afterward, a depthwise Conv layer is employed. The kernel size of the depthwise Conv layer is (18, 1) and (15, 1) for the sensor domain and source domain input features, respectively, due to the variation in input channels. Batch normalization is applied following both Conv layers. The linear activation function is utilized with the 2D CNN layer, while the Exponential Linear Unit (ELU) activation function is used for the depthwise CNN layer. The weights of the depthwise CNN layer are regularized with a maximum norm weight constraint of 1. A 2D average pooling layer with the size of (1, 2) is employed at the output stage along with a dropout layer with a rate of 0.5 to regularize the decoder. The second stage of the decoder included a separable Conv layer with 96 filters, each of size (1, 16), a batch normalization layer, and an activation function layer with ELU activation function. Subsequently, a 2D average pooling layer is applied with a size of (1, 4), and a feature vector is obtained by flattening the output of the average pooling layer. Further, the feature vector is fed to the output dense layer consisting of three neurons and the linear activation function. The incorporation of depthwise and separable Conv layers results in a significant reduction in the model parameter count, rendering a more compact model. Table I shows the model architecture details for sensor domain input features.

2) *rDeepConvNet*: DeepConvNet model includes a total of four convolution blocks. The first block of the model consists of two 2D Conv layers followed by a batch normalization layer and an activation layer with the ELU activation function. The first Conv layer has the size of (1, 5); however, the kernel size of the second Conv layer is (18, 1) and (15, 1) for sensor domain and source domain input features, respectively. The remaining three blocks have identical configurations, with each block consisting of a 2D Conv layer of kernel size (1, 5), a batch normalization layer, and an activation layer with an ELU activation layer. The last block is followed by a 2D Max-pooling layer of kernel size and stride (1, 2). Each Conv layer consists of 25 filters in the first block; the number of filters in subsequent blocks is doubled, as shown in Table II. The fourth block output is flattened and fed to the output dense layer with three neurons and linear activation.

3) *rShallowConvNet*: The ShallowConvNet model consists of two 2D Conv layers with 40 filters and the linear activation function. The first 2D Conv layer has a kernel size of (1, 13), while the kernel size of the second Conv layer is (18, 1) and (15, 1) for sensor and source domain input features, respectively. The output of the Conv layers undergoes batch normalization, followed by the application of the square activation function. Subsequently, a 2D average-pooling layer of kernel size and stride (1, 5) and (1, 2), respectively, is utilized along with a logarithmic activation function. Further, the output of the average pooling layer is flattened to a vector and fed to the output-dense layer with three neurons with the linear activation function. A dropout layer with a drop rate of 0.5 is implemented to prevent overfitting.

TABLE I  
MODEL ARCHITECTURE OF REEGNET DECODER FOR EEG  
SENSOR-DOMAIN FEATURES INPUT.

Layer	Kernel Size	# of filters	Layer Parameters
Conv2D	(1, 32)	32	Stride = (1, 1), Activation = Linear
BatchNorm	-	-	-
DepthwiseConv2D	(18, 1)	-	Depth multiplier = 3
BatchNorm	-	-	-
Activation	-	-	Activation = ELU
AveragePooling2D	(1, 2)	-	Stride = (1, 2)
Dropout	-	-	Dropout Rate = 0.5
SeperableConv2D	(1, 16)	96	Zero Padding
BatchNorm	-	-	-
Activation	-	-	Activation = ELU
AveragePooling2D	(1, 4)	-	Stride = (1, 4)
Dropout	-	-	Dropout Rate = 0.5
Flatten	-	-	-
Dense	-	-	Neurons = 3, Activation = Linear

TABLE II  
MODEL ARCHITECTURE OF RDEEPCONVNET DECODER FOR EEG  
SENSOR-DOMAIN FEATURES INPUT.

Layer	Kernel Size	# of filters	Layer Parameters
Conv2D	(1, 5)	25	Stride = (1, 1), Activation = Linear
Conv2D	(18, 1)	25	Stride = (1, 1), Activation = Linear
BatchNorm	-	-	-
Activation	-	-	Activation = ELU
Dropout	-	-	Dropout Rate = 0.5
Conv2D	(1, 5)	50	Stride = (1, 1), Activation = Linear
BatchNorm	-	-	-
Activation	-	-	Activation = ELU
Dropout	-	-	Dropout Rate = 0.5
Conv2D	(1, 5)	100	Stride = (1, 1), Activation = Linear
BatchNorm	-	-	-
Activation	-	-	Activation = ELU
Dropout	-	-	Dropout Rate = 0.5
Conv2D	(1, 5)	200	Stride = (1, 1), Activation = Linear
BatchNorm	-	-	-
Activation	-	-	Activation = ELU
MaxPooling2D	(1, 2)	-	Stride = (1, 2)
Dropout	-	-	Dropout Rate = 0.5
Flatten	-	-	-
Dense	-	-	Neurons = 3, Activation = Linear

TABLE III  
MODEL ARCHITECTURE OF RSHALLOWCONVNET DECODER FOR EEG  
SENSOR-DOMAIN FEATURES INPUT.

Layer	Kernel Size	# of filters	Layer Parameters
Conv2D	(1, 13)	40	Stride = (1, 1), Activation = Linear
Conv2D	(18, 1)	40	Stride = (1, 1), Activation = Linear
BatchNorm	-	-	-
Activation	-	-	Activation = Square
AveragePooling2D	(1, 5)	-	Stride = (1, 2)
Activation	-	-	Activation = log
Dropout	-	-	Dropout Rate = 0.5
Flatten	-	-	-
Dense	-	-	Neurons = 3, Activation = Linear

### E. Experimental Details

The data normalization is performed on the EEG sensor and source time series using the z-score normalization technique, depicted as

$$V^n[t] = \frac{v^n[t] - \Pi_{v_n}}{\rho_{v_n}} \quad (2)$$

where, at time instant  $t$ ,  $v^n[t]$  and  $V^n[t]$  are the  $n^{th}$  channel denoised and normalized signal, respectively.  $\Pi_{v_n}$  and  $\rho_{v_n}$  denotes the mean and standard deviation of the  $v^n$  signal, respectively.

Normalized sensor and source domain time series are utilized as input to neural decoders. For each trial, hand kinematics data is utilized from the movement initiation until

the participant reinstated the hand to the initial resting position. Time-lagged EEG sensors and source time series segments that included the pre-motor neural information for hand trajectory decoding are utilized. This study considered various window sizes (250 ms to 450 ms) and lags (50 ms to 200 ms) with EEG data up to 650 ms prior to movement onset for the decoding analysis. The input to the neural decoders was a 2D matrix of dimension  $C \times W$ , where  $C$  is the number of selected channels and  $W$  is the window size. The number of selected channels ( $C$ ) for the sensor and source domain time series are 18 and 15, respectively.

The dataset is divided into three data subsets for the performance evaluation of the neural decoders: training, validation, and test datasets. Model training is performed using the training dataset, while the validation dataset is utilized for tuning model hyper-parameters and avoiding over-fitting. The performance of the trained model was evaluated on the test dataset. Data corresponding to 294 trials is available for each participant in the WAY-EEG-GAL dataset. For intra-subject decoding analysis, the data for each participant is subdivided into training, validation, and test data corresponding to 234 trials, 30 trials, and 30 trials, respectively. For inter-subject decoding analysis, a 4-fold cross-validation strategy is adopted. Training and validation are carried out using data from nine subjects, and the trained model is evaluated using data corresponding to the remaining three subjects. The model training is performed using a mini-batch training process with a batch size of 64. The mean-squared error (mse) loss is minimized using the Adam optimization algorithm to define model parameters. The model undergoes training for a maximum of 400 epochs, and to prevent overfitting, early stopping is implemented based on the validation set mse loss, with a patience of 5 epochs.

## III. RESULTS AND DISCUSSION

### A. Performance Metric

The Pearson correlation coefficient (PCC) is employed as a performance metric for evaluating the MKP efficacy of the decoding models. This coefficient is calculated across measured and predicted kinematics trajectory, representing linear correlation with output values in the range  $[-1, 1]$ . A PCC value of -1 and +1 indicates a strong negative and positive correlation, respectively, while a PCC value of 0 represents no correlation. The mathematical expression that represents the Pearson correlation coefficient between the measured ( $C_x$ ) and estimated ( $C_y$ ) is depicted as follows:

$$\Pi(C_x, C_y) = \frac{1}{T-1} \sum_{i=1}^T \left( \frac{C_x^i - \alpha_{C_x}}{\beta_{C_x}} \right) \left( \frac{C_y^i - \alpha_{C_y}}{\beta_{C_y}} \right) \quad (3)$$

where,  $\alpha_m$  and  $\beta_m$  are the mean and standard deviation of  $m$ , respectively, with  $m \in \{C_x, C_y\}$ .

### B. Results

In the first set of experiments, the performance of motor kinematics prediction is explored for intra-subject settings

TABLE IV  
MEAN PCC VALUES FOR INTRA-SUBJECT TRAJECTORY DECODING IN THE X, Y, AND Z DIRECTIONS USING EEG SENSOR-DOMAIN AND SOURCE-DOMAIN TIME SERIES INPUT. THE EFFECT ON PCC VALUES USING DIFFERENT EEG LAG AND WINDOW SIZES WITH DIFFERENT DECODING MODELS IS ALSO DEPICTED.

Direction	Decoders	EEG Lag	Sensor Domain					Source Domain				
			EEG Window					EEG Window				
			250	300	350	400	450	250	300	350	400	450
x	mLR	50	0.340	0.351	0.369	0.374	0.385	0.410	0.420	0.429	0.429	0.433
		100	0.333	0.353	0.361	0.374	0.395	0.402	0.414	0.417	0.423	0.451
		150	0.335	0.346	0.361	0.383	0.384	0.396	0.402	0.411	0.441	0.442
		200	0.329	0.346	0.369	0.372	0.382	0.384	0.396	0.429	0.431	0.431
	rSCNet	50	0.731	0.734	0.727	0.723	0.714	0.706	0.707	0.710	0.698	0.692
		100	0.736	0.734	0.730	0.717	0.723	0.709	0.710	0.706	0.704	0.700
		150	0.744	0.735	0.726	0.725	0.717	0.713	0.706	0.701	0.705	0.699
		200	0.738	0.726	0.727	0.722	0.715	0.708	0.696	0.702	0.692	0.683
	rDCNet	50	0.741	0.752	0.745	0.715	0.722	0.717	0.732	0.731	0.718	0.715
		100	0.746	0.752	0.741	0.730	0.724	0.722	0.723	0.722	0.707	0.707
		150	0.752	0.741	0.744	0.739	0.702	0.722	0.730	0.717	0.715	0.704
		200	0.734	0.743	0.743	0.733	0.715	0.716	0.718	0.730	0.708	0.703
	rEEGNet	50	0.781	0.783	0.787	0.785	0.785	0.753	0.766	0.769	0.767	0.753
		100	0.785	0.781	0.785	0.781	<b>0.790</b>	0.761	0.768	0.758	0.759	<b>0.769</b>
		150	0.781	0.781	0.780	0.788	0.781	0.758	0.758	0.755	0.767	0.766
200		0.783	0.777	0.787	0.779	0.779	0.760	0.751	0.765	0.759	0.760	
y	mLR	50	0.349	0.358	0.377	0.379	0.392	0.416	0.427	0.436	0.434	0.438
		100	0.340	0.361	0.366	0.382	0.401	0.407	0.420	0.422	0.429	0.458
		150	0.342	0.351	0.369	0.390	0.388	0.401	0.407	0.417	0.448	0.446
		200	0.333	0.354	0.376	0.377	0.387	0.388	0.403	0.436	0.436	0.435
	rSCNet	50	0.738	0.742	0.736	0.735	0.727	0.711	0.715	0.719	0.711	0.708
		100	0.743	0.741	0.738	0.728	0.733	0.717	0.720	0.714	0.711	0.709
		150	0.749	0.740	0.735	0.736	0.729	0.721	0.712	0.710	0.715	0.706
		200	0.743	0.732	0.736	0.728	0.725	0.714	0.704	0.711	0.705	0.697
	rDCNet	50	0.753	0.763	0.762	0.751	0.754	0.727	0.741	0.742	0.734	0.733
		100	0.754	0.761	0.760	0.754	0.756	0.733	0.735	0.731	0.730	0.736
		150	0.760	0.751	0.757	0.755	0.744	0.731	0.738	0.729	0.736	0.734
		200	0.743	0.752	0.755	0.753	0.750	0.725	0.725	0.739	0.730	0.730
	rEEGNet	50	0.787	0.788	0.792	0.787	0.789	0.759	0.774	0.775	0.773	0.761
		100	0.789	0.788	0.788	0.786	<b>0.795</b>	0.768	0.774	0.763	0.768	<b>0.777</b>
		150	0.786	0.783	0.782	0.793	0.784	0.764	0.764	0.762	0.776	0.773
200		0.787	0.780	0.791	0.785	0.782	0.766	0.756	0.771	0.767	0.767	
z	mLR	50	0.156	0.158	0.164	0.169	0.173	0.289	0.296	0.296	0.301	0.304
		100	0.153	0.159	0.164	0.167	0.173	0.287	0.289	0.293	0.297	0.298
		150	0.154	0.160	0.162	0.167	0.173	0.281	0.285	0.289	0.290	0.290
		200	0.155	0.157	0.163	0.168	0.170	0.277	0.281	0.283	0.282	0.287
	rSCNet	50	0.562	0.565	0.564	0.560	0.545	0.568	0.578	0.580	0.582	0.576
		100	0.559	0.562	0.555	0.555	0.549	0.576	0.579	0.578	0.574	0.583
		150	0.565	0.558	0.550	0.559	0.551	0.584	0.576	0.569	0.581	0.577
		200	0.553	0.549	0.553	0.543	0.530	0.575	0.571	0.581	0.572	0.565
	rDCNet	50	0.540	0.564	0.559	0.537	0.549	0.570	0.601	0.610	0.603	0.596
		100	0.547	0.571	0.561	0.557	0.542	0.572	0.593	0.601	0.588	0.597
		150	0.548	0.557	0.566	0.575	0.520	0.586	0.599	0.591	0.606	0.587
		200	0.533	0.558	0.569	0.552	0.529	0.576	0.590	0.609	0.590	0.592
	rEEGNet	50	0.601	0.608	0.625	0.624	0.624	0.620	0.633	0.639	0.640	0.635
		100	0.597	0.607	0.617	0.616	<b>0.637</b>	0.627	0.632	0.633	0.634	<b>0.647</b>
		150	0.604	0.598	0.609	0.626	0.624	0.616	0.626	0.621	0.645	0.640
200		0.599	0.601	0.617	0.611	0.616	0.620	0.613	0.639	0.637	0.639	

Note: the bold entries represent the highest PCC value obtained in the x, y, and z directions for the EEG sensor-domain and source-domain input features.  
rDCNet - rDeepConvNet, rSCNet - rShallowConvNet

using sensor-domain and source-domain EEG features. Table IV presents the mean correlation values for twelve subjects using different decoding models. The decoding analysis is performed for hand kinematics trajectory in the x, y, and z-directions. In addition, the effect of EEG lag and window size is also presented in Table IV. EEG lag up to 200 ms is analyzed with various EEG window sizes in the range of 250 – 450 ms.

Furthermore, the performance analysis for inter-subject decoding is also explored. The mean correlation values across twelve subjects using the mLR model and three deep learning models are presented in Table V. The decoding analysis is

performed for 50 ms time lag and window size up to 450 ms for the MKP of hand position in x, y, and z-directions. In particular, sensor-domain and source-domain EEG features are utilized for comparing MKP performance.

### C. Discussion

1) *mLR Performance analysis*: In this work, the mLR model is utilized for MKP using EEG sensor-domain and source-domain features for hand trajectory in x, y, and z-directions. The decoding performance is evaluated for intra-subject and inter-subject decoding settings as shown in Table IV and V, respectively. In intra-subject decoding analysis, the

TABLE V  
MEAN PCC VALUES FOR INTER-SUBJECT TRAJECTORY DECODING IN THE X, Y, AND Z DIRECTIONS USING EEG SENSOR-DOMAIN AND SOURCE-DOMAIN TIME SERIES INPUT. THE EFFECT ON PCC VALUES USING 50 MS LAG AND DIFFERENT WINDOW SIZES WITH DIFFERENT DECODING MODELS IS ALSO DEPICTED.

Direction	Decoders	Sensor Domain					Source Domain				
		Window size (ms)					Window size (ms)				
		250	300	350	400	450	250	300	350	400	450
x	mLR	0.143	0.151	0.168	0.186	0.203	0.150	0.150	0.167	0.182	0.201
	rSCNet	0.685	0.692	0.691	0.694	0.692	0.625	0.625	0.627	0.621	0.633
	rDCNet	0.730	0.731	0.731	0.731	0.715	0.664	0.658	0.658	0.652	0.643
	rEEGNet	0.745	0.744	0.749	<b>0.753</b>	0.748	0.683	0.682	<b>0.684</b>	0.683	0.683
y	mLR	0.145	0.156	0.172	0.188	0.203	0.158	0.160	0.176	0.188	0.204
	rSCNet	0.688	0.694	0.697	0.703	0.695	0.627	0.629	0.628	0.621	0.636
	rDCNet	0.729	0.731	0.731	0.733	0.714	0.668	0.664	0.660	0.656	0.643
	rEEGNet	0.745	0.743	0.750	<b>0.756</b>	0.744	0.685	0.686	<b>0.687</b>	<b>0.687</b>	0.680
z	mLR	0.051	0.051	0.048	0.047	0.047	0.146	0.144	0.142	0.147	0.149
	rSCNet	0.412	0.407	0.391	0.402	0.419	0.431	0.442	0.448	0.445	0.453
	rDCNet	0.442	0.445	0.455	0.468	0.465	0.468	0.473	0.491	0.497	0.493
	rEEGNet	0.465	0.454	0.461	0.478	<b>0.490</b>	0.484	0.495	<b>0.515</b>	0.506	0.509

Note: the bold entries represent the highest PCC value obtained in the x, y, and z directions for the EEG sensor-domain and source-domain input features.  
rDCNet - rDeepConvNet, rSCNet - rShallowConvNet

mLR with source-domain EEG features has better decoding performance in x, y, and z-directions in comparison with sensor-domain-based MKP. The same can be depicted from  $p$ -values shown in Table VI. However, the decoding performance degrades in the case of inter-subject decoding. Also, the decoding performance is statistically similar using the EEG sensor-domain and source-domain features for MKP, as shown in Table VI. Furthermore, the deep learning-based decoders outperformed the mLR model with sensor-domain and source-domain features in intra-subject and inter-subject settings, as depicted from the  $p$ -values shown in Table VII-VI.

2) *Deep Learning Model Analysis*: Three deep learning models, namely, rShallowConvNet, rDeepConvNet, and rEEGNet, are utilized to access the MKP performance during the grasp-and-lift task. As evident from the results in Tables IV - V, the rEEGNet decoding model outperforms the models for MKP in the x, y, and z-directions. The model architecture consists of depthwise and separable convolution layers that are designed for feature extraction from EEG data within end-to-end model training. Further, rEEGNet has the minimum parameters to train among the deep learning models utilized for MKP analysis. Subsequently, a detailed  $t$ -test is performed to compare the trajectory decoding performance of the various decoding models. The statistical analysis is performed to compare the decoding performance of models with sensor-domain features and source-domain input features. The results of the  $t$ -test are shown in Table VII for the intra-subject decoding case. It can be noted that the deep learning-based decoders performed significantly better than the traditionally used mLR model. In particular, the rEEGNet model decoding performance is statistically better in comparison to other decoding models. For the inter-subject case, all  $p$ -values are  $< 0.05$  in the  $t$ -test, which signifies the superior performance of the rEEGNet model over the other decoding models.

3) *EEG Lag Analysis*: In this analysis, hand trajectory is decoded using pre-movement EEG data with distinct window sizes and lags. For intra-subject decoding analysis, EEG segment up to 200  $ms$  prior to movement-onset and size in the 250 – 450  $ms$  range is utilized as shown in Table

IV. The best correlation values are obtained for an EEG lag of 100  $ms$  and window size of 450  $ms$  while using the rEEGNet decoding model. For sensor-domain EEG features, the mean correlation values obtained are 0.790, 0.795, and 0.637 for x, y, and z-directions, respectively, while the mean correlation values of 0.769, 0.777, and 0.647 are observed with EEG source-domain features. In the case of inter-subject decoding analysis, EEG segments with varying sizes and 50  $ms$  pre-movement EEG data are taken as depicted in Table V. The rEEGNet model has the best decoding performance with sensor-domain as well as source-domain input features. With sensor-domain input features, the best mean correlation values of 0.753 and 0.756 are observed with 400  $ms$  window size in the x and y directions, respectively, while 0.490 mean correlation value is obtained with 450  $ms$  window size in the z-direction. The decoding performance with source-domain features is observed with 350  $ms$  window size and mean correlation values of 0.684, 0.687, and 0.515 in the x, y, and z-directions, respectively.

4) *Sensor-domain and Source-domain Feature Analysis*: EEG sensor-domain and source-domain features are employed as inputs to the decoding models to access the suitable features for MKD during the grasp-and-lift task. In intra-subject decoding analysis, the highest correlation values are obtained by deep learning models while using EEG sensor-domain features in x and y-direction decoding. However, in z-direction, the decoding performance of the models is better with EEG source-domain features. In particular, the rEEGNet neural decoder performs best with both sensor-domain and source-domain features as input. In inter-subject decoding analysis, it is observed that the best correlation values are obtained using sensor-domain EEG features with the rEEGNet decoder. However, the rEEGNet model with source-domain features has better decoding performance in the z-direction. A detailed  $t$ -test is performed to compare the decoding performance between the decoding models with EEG sensor-domain and source-domain input features. The results of the  $t$ -test are shown in Table VI in the form of  $p$ -values for intra-subject and inter-subject settings.

TABLE VI

$p$  VALUES OF ONE-TAILED  $t$ -TEST BETWEEN SENSOR-DOMAIN AND SOURCE-DOMAIN FEATURES-BASED TRAJECTORY DECODERS FOR INTRA-SUBJECT AND INTER-SUBJECT SETTINGS IN THE X, Y, AND Z DIRECTIONS.

Intra-Subject						Inter-Subject					
x-direction		Source Domain				x-direction		Source Domain			
		mLR	rSCNet	rDCNet	rEEGNet			mLR	rSCNet	rDCNet	rEEGNet
Sensor Domain	mLR	$7.40 \times 10^{-5}$	$2.93 \times 10^{-6}$	$1.58 \times 10^{-6}$	$6.45 \times 10^{-7}$	Sensor Domain	mLR	$4.32 \times 10^{-1}$	$7.54 \times 10^{-7}$	$2.32 \times 10^{-6}$	$5.82 \times 10^{-7}$
	rSCNet	$9.35 \times 10^{-7}$	$1.14 \times 10^{-4}$	$2.09 \times 10^{-1}$	$4.51 \times 10^{-4}$		rSCNet	$2.64 \times 10^{-7}$	$5.80 \times 10^{-6}$	$7.59 \times 10^{-4}$	$2.48 \times 10^{-3}$
	rDCNet	$3.03 \times 10^{-6}$	$9.98 \times 10^{-4}$	$3.09 \times 10^{-2}$	$1.08 \times 10^{-2}$		rDCNet	$6.96 \times 10^{-7}$	$1.55 \times 10^{-5}$	$1.75 \times 10^{-6}$	$6.57 \times 10^{-5}$
	rEEGNet	$1.76 \times 10^{-8}$	$1.18 \times 10^{-5}$	$3.37 \times 10^{-5}$	$1.08 \times 10^{-3}$		rEEGNet	$1.57 \times 10^{-7}$	$1.01 \times 10^{-6}$	$1.75 \times 10^{-5}$	$6.85 \times 10^{-7}$
y-direction		Source Domain				y-direction		Source Domain			
		mLR	rSCNet	rDCNet	rEEGNet			mLR	rSCNet	rDCNet	rEEGNet
Sensor Domain	mLR	$6.87 \times 10^{-5}$	$1.11 \times 10^{-6}$	$6.08 \times 10^{-7}$	$5.56 \times 10^{-7}$	Sensor Domain	mLR	$6.22 \times 10^{-2}$	$7.11 \times 10^{-7}$	$2.35 \times 10^{-6}$	$6.30 \times 10^{-7}$
	rSCNet	$3.81 \times 10^{-7}$	$1.47 \times 10^{-4}$	$4.94 \times 10^{-1}$	$2.19 \times 10^{-4}$		rSCNet	$1.32 \times 10^{-7}$	$3.88 \times 10^{-5}$	$1.48 \times 10^{-3}$	$5.66 \times 10^{-3}$
	rDCNet	$1.25 \times 10^{-7}$	$4.71 \times 10^{-6}$	$7.12 \times 10^{-5}$	$7.36 \times 10^{-3}$		rDCNet	$5.22 \times 10^{-7}$	$2.82 \times 10^{-5}$	$5.41 \times 10^{-6}$	$1.97 \times 10^{-5}$
	rEEGNet	$3.04 \times 10^{-8}$	$5.20 \times 10^{-7}$	$1.29 \times 10^{-5}$	$1.69 \times 10^{-3}$		rEEGNet	$1.33 \times 10^{-7}$	$6.51 \times 10^{-6}$	$2.94 \times 10^{-5}$	$2.92 \times 10^{-6}$
z-direction		Source Domain				z-direction		Source Domain			
		mLR	rSCNet	rDCNet	rEEGNet			mLR	rSCNet	rDCNet	rEEGNet
Sensor Domain	mLR	$1.36 \times 10^{-8}$	$5.27 \times 10^{-9}$	$1.07 \times 10^{-7}$	$3.12 \times 10^{-9}$	Sensor Domain	mLR	$3.64 \times 10^{-7}$	$4.96 \times 10^{-8}$	$1.79 \times 10^{-7}$	$1.22 \times 10^{-7}$
	rSCNet	$6.54 \times 10^{-7}$	$6.59 \times 10^{-3}$	$4.19 \times 10^{-3}$	$7.17 \times 10^{-5}$		rSCNet	$1.40 \times 10^{-7}$	$1.96 \times 10^{-3}$	$3.88 \times 10^{-4}$	$2.14 \times 10^{-4}$
	rDCNet	$8.18 \times 10^{-7}$	$3.18 \times 10^{-3}$	$8.72 \times 10^{-4}$	$5.79 \times 10^{-5}$		rDCNet	$1.75 \times 10^{-7}$	$1.35 \times 10^{-2}$	$3.59 \times 10^{-5}$	$1.46 \times 10^{-4}$
	rEEGNet	$2.93 \times 10^{-8}$	$1.39 \times 10^{-4}$	$4.68 \times 10^{-3}$	$8.93 \times 10^{-4}$		rEEGNet	$2.31 \times 10^{-7}$	$4.56 \times 10^{-3}$	$2.25 \times 10^{-2}$	$4.56 \times 10^{-3}$

rDCNet - rDeepConvNet, rSCNet - rShallowConvNet

TABLE VII

$p$  VALUES OF ONE-TAILED  $t$ -TEST BETWEEN TRAJECTORY DECODING MODELS WITH SENSOR-DOMAIN AND SOURCE-DOMAIN FEATURES FOR INTRA-SUBJECT SETTING IN THE X, Y, AND Z DIRECTIONS.

Sensor-domain					Source-domain				
x-direction					x-direction				
	mLR	rSCNet	rDCNet	rEEGNet		mLR	rSCNet	rDCNet	rEEGNet
mLR	-	$2.90 \times 10^{-6}$	$6.00 \times 10^{-6}$	$2.66 \times 10^{-7}$	mLR	-	$8.69 \times 10^{-7}$	$3.38 \times 10^{-7}$	$9.79 \times 10^{-8}$
rSCNet	$2.90 \times 10^{-6}$	-	$5.91 \times 10^{-2}$	$7.46 \times 10^{-5}$	rSCNet	$8.69 \times 10^{-7}$	-	$6.43 \times 10^{-4}$	$3.99 \times 10^{-5}$
rDCNet	$6.00 \times 10^{-6}$	$5.91 \times 10^{-2}$	-	$1.56 \times 10^{-3}$	rDCNet	$3.38 \times 10^{-7}$	$6.43 \times 10^{-4}$	-	$5.94 \times 10^{-5}$
rEEGNet	$2.66 \times 10^{-7}$	$7.46 \times 10^{-5}$	$1.56 \times 10^{-3}$	-	rEEGNet	$9.79 \times 10^{-8}$	$3.99 \times 10^{-5}$	$5.94 \times 10^{-5}$	-
y-direction					y-direction				
	mLR	rSCNet	rDCNet	rEEGNet		mLR	rSCNet	rDCNet	rEEGNet
mLR	-	$1.55 \times 10^{-6}$	$7.72 \times 10^{-7}$	$2.98 \times 10^{-7}$	mLR	-	$1.73 \times 10^{-7}$	$6.20 \times 10^{-8}$	$7.57 \times 10^{-8}$
rSCNet	$1.55 \times 10^{-6}$	-	$5.43 \times 10^{-4}$	$2.04 \times 10^{-5}$	rSCNet	$1.73 \times 10^{-7}$	-	$1.04 \times 10^{-4}$	$8.73 \times 10^{-6}$
rDCNet	$7.72 \times 10^{-7}$	$5.43 \times 10^{-4}$	-	$6.94 \times 10^{-5}$	rDCNet	$6.20 \times 10^{-8}$	$1.04 \times 10^{-4}$	-	$3.03 \times 10^{-5}$
rEEGNet	$2.98 \times 10^{-7}$	$2.04 \times 10^{-5}$	$6.94 \times 10^{-5}$	-	rEEGNet	$7.57 \times 10^{-8}$	$8.73 \times 10^{-6}$	$3.03 \times 10^{-5}$	-
z-direction					z-direction				
	mLR	rSCNet	rDCNet	rEEGNet		mLR	rSCNet	rDCNet	rEEGNet
mLR	-	$1.88 \times 10^{-7}$	$2.55 \times 10^{-7}$	$3.13 \times 10^{-9}$	mLR	-	$9.95 \times 10^{-9}$	$3.98 \times 10^{-7}$	$8.13 \times 10^{-9}$
rSCNet	$1.88 \times 10^{-7}$	-	$7.89 \times 10^{-2}$	$6.33 \times 10^{-4}$	rSCNet	$9.95 \times 10^{-9}$	-	$7.53 \times 10^{-3}$	$7.97 \times 10^{-7}$
rDCNet	$2.55 \times 10^{-7}$	$7.89 \times 10^{-2}$	-	$3.55 \times 10^{-4}$	rDCNet	$3.98 \times 10^{-7}$	$7.53 \times 10^{-3}$	-	$2.52 \times 10^{-4}$
rEEGNet	$3.13 \times 10^{-9}$	$6.33 \times 10^{-4}$	$3.55 \times 10^{-4}$	-	rEEGNet	$8.13 \times 10^{-9}$	$7.97 \times 10^{-7}$	$2.52 \times 10^{-4}$	-

rDCNet - rDeepConvNet, rSCNet - rShallowConvNet

5) *Intra-subject and Inter-subject Decoding Analysis*: The objective of the intra-subject and inter-subject decoding analysis is to explore the subject-specific and subject-independent feature-learning capabilities of the decoding model for the kinematics trajectory prediction during the grasp-and-lift task. It can be noted that the decoding model, in particular rEEGNet, is able to learn subject-specific features for MKP with sensor-domain as well as source-domain EEG features as input during the grasp-and-lift task, as can be depicted from the results in Table IV. The mean correlation values of 0.741 and 0.731 across three axes are obtained, with 100 ms EEG lag and 450 ms window size for sensor-domain and source-domain features as decoder input, respectively. We can conclude that the rEEGNet model can learn the subject-specific motor information from the EEG sensor-domain and source-domain

features for MKP.

In inter-subject decoding analysis, subject-independent features are learned by the decoding models, and the performance evaluation is done on the subject data that is excluded from the training phase. The rEEGNet model with sensor-domain input features has the best decoding performance in the x and y directions. However, in the z-direction, source-domain input features based rEEGNet have better decoding performance, as shown in Table VI.

#### IV. CONCLUSION

This study explores the EEG source imaging-based kinematics decoding using a deep learning-based decoding model. In particular, the frontoparietal regions are selected for the MKP during the grasp-and-lift task. The motor-related in-



formation encoded in the pre-movement brain activation is utilized for hand trajectory decoding using the time-lagged EEG features in sensor and source domains. The MKP analysis is performed using the convolutional neural network-based decoding models. Further, inter-subject decoding analysis has been performed to evaluate the subject-independent feature-learning capabilities of the decoding models. The proposed rEEGNet yielded the overall best kinematics decoding performance using the EEG sensor-domain features. The Pearson correlation coefficient (PCC) is used as a performance metric for MKP. The decoding analysis shows the viability of continuous trajectory decoding using EEG source domain features. However, the decoding accuracy using the sensor-domain EEG features is better than the source-domain counterpart using the proposed decoding model.

#### ACKNOWLEDGMENT

The authors would like to thank Prof. Sitikantha Roy and Prof. Shubhendu Bhasin from the Indian Institute of Technology Delhi and Dr. Suriya Prakash from All India Institute of Medical Sciences Delhi for their constructive comments during the preparation of the manuscript.

#### REFERENCES

- [1] J. R. Wolpaw, J. D. R. Millan, and N. F. Ramsey, "Brain-computer interfaces: Definitions and principles," *Handbook of clinical neurology*, vol. 168, pp. 15–23, 2020.
- [2] R. Mane, T. Chouhan, and C. Guan, "BCI for stroke rehabilitation: motor and beyond," *Journal of neural engineering*, vol. 17, no. 4, p. 041001, 2020.
- [3] A. Miladinović, M. Ajčević, P. Busan, J. Jarmolowska, G. Silveri, M. Deodato, S. Mezzarobba, P. P. Battaglini, and A. Accardo, "Evaluation of Motor Imagery-Based BCI methods in neurorehabilitation of Parkinson's Disease patients," in *2020 42nd Annual International Conference of the IEEE Engineering in Medicine & Biology Society (EMBC)*. IEEE, 2020, pp. 3058–3061.
- [4] R. Na, C. Hu, Y. Sun, S. Wang, S. Zhang, M. Han, W. Yin, J. Zhang, X. Chen, and D. Zheng, "An embedded lightweight SSVEP-BCI electric wheelchair with hybrid stimulator," *Digital Signal Processing*, vol. 116, p. 103101, 2021.
- [5] L. Cao, W. Wang, C. Huang, Z. Xu, H. Wang, J. Jia, S. Chen, Y. Dong, C. Fan, and V. H. C. de Albuquerque, "An effective fusing approach by combining connectivity network pattern and temporal-spatial analysis for EEG-based BCI rehabilitation," *IEEE Transactions on Neural Systems and Rehabilitation Engineering*, vol. 30, pp. 2264–2274, 2022.
- [6] J. M. Catalán, E. Trigili, M. Nann, A. Blanco-Ivorra, C. Lauretti, F. Cordella, E. Ivorra, E. Armstrong, S. Crea, M. Alcañiz *et al.*, "Hybrid brain/neural interface and autonomous vision-guided whole-arm exoskeleton control to perform activities of daily living (ADLs)," *Journal of NeuroEngineering and Rehabilitation*, vol. 20, no. 1, p. 61, 2023.
- [7] P. Demarest, N. Rustamov, J. Swift, T. Xie, M. Adamek, H. Cho, E. Wilson, Z. Han, A. Belsten, N. Luczak *et al.*, "A novel theta-controlled vibrotactile brain-computer interface to treat chronic pain: a pilot study," *Scientific Reports*, vol. 14, no. 1, p. 3433, 2024.
- [8] A. Hekmatmanesh, P. H. Nardelli, and H. Handroos, "Review of the state-of-the-art of brain-controlled vehicles," *IEEE Access*, vol. 9, pp. 110 173–110 193, 2021.
- [9] A. Nijholt, J. L. Contreras-Vidal, C. Jeunet, and A. Väljamäe, "Brain-computer interfaces for non-clinical (home, sports, art, entertainment, education, well-being) applications," *Frontiers in Computer Science*, vol. 4, p. 860619, 2022.
- [10] S. Moreno-Calderón, V. Martínez-Cagigal, E. Santamaría-Vázquez, S. Pérez-Velasco, D. Marcos-Martínez, and R. Hornero, "Assessing the Potential of Brain-Computer Interface Multiplayer Video Games using c-VEPs: A Pilot Study," in *2023 45th Annual International Conference of the IEEE Engineering in Medicine & Biology Society (EMBC)*. IEEE, 2023, pp. 1–4.
- [11] N. Robinson, R. Mane, T. Chouhan, and C. Guan, "Emerging trends in BCI-robotics for motor control and rehabilitation," *Current Opinion in Biomedical Engineering*, vol. 20, p. 100354, 2021.
- [12] J. d. R. Millán, "Invasive or noninvasive: understanding brain-machine interface technology," *IEEE Engineering in Medicine and Biology Magazine*, vol. 29, no. 1, pp. 16–22, 2010.
- [13] K. J. Miller, D. Hermes, and N. P. Staff, "The current state of electrocorticography-based brain-computer interfaces," *Neurosurgical focus*, vol. 49, no. 1, p. E2, 2020.
- [14] N. Naseer and K.-S. Hong, "fNIRS-based brain-computer interfaces: a review," *Frontiers in human neuroscience*, vol. 9, p. 3, 2015.
- [15] X. Wang, Y. Zheng, F. Wang, H. Ding, J. Meng, and Y. Zhuo, "Unilateral movement decoding of upper and lower limbs using magnetoencephalography," *Biomedical Signal Processing and Control*, vol. 93, p. 106215, 2024.
- [16] H. I. Baqapuri, L. D. Roes, M. Zvyagintsev, S. Ramadan, M. Keller, E. Roecher, J. Zweerings, M. Klasen, R. C. Gur, and K. Mathiak, "A novel brain-computer interface virtual environment for neurofeedback during functional MRI," *Frontiers in Neuroscience*, vol. 14, p. 593854, 2021.
- [17] X. Gu, Z. Cao, A. Jolfaei, P. Xu, D. Wu, T.-P. Jung, and C.-T. Lin, "EEG-based brain-computer interfaces (BCIs): A survey of recent studies on signal sensing technologies and computational intelligence approaches and their applications," *IEEE/ACM transactions on computational biology and bioinformatics*, vol. 18, no. 5, pp. 1645–1666, 2021.
- [18] Y. Zheng, Y. Ma, J. Cammon, S. Zhang, J. Zhang, and Y. Zhang, "A new feature selection approach for driving fatigue EEG detection with a modified machine learning algorithm," *Computers in Biology and Medicine*, vol. 147, p. 105718, 2022.
- [19] A. Othmani, A. Q. M. Sabri, S. Aslan, F. Chaieb, H. Rameh, R. Alfred, and D. Cohen, "EEG-based neural networks approaches for fatigue and drowsiness detection: A survey," *Neurocomputing*, p. 126709, 2023.
- [20] X. Li, Y. Zhang, P. Tiwari, D. Song, B. Hu, M. Yang, Z. Zhao, N. Kumar, and P. Marttinen, "EEG based emotion recognition: A tutorial and review," *ACM Computing Surveys*, vol. 55, no. 4, pp. 1–57, 2022.
- [21] M. Jafari, A. Shoeb, M. Khodatars, S. Bagherzadeh, A. Shalhaf, D. L. García, J. M. Gorriz, and U. R. Acharya, "Emotion recognition in EEG signals using deep learning methods: A review," *Computers in Biology and Medicine*, p. 107450, 2023.
- [22] Z. Tang, H. Wang, Z. Cui, X. Jin, L. Zhang, Y. Peng, and B. Xing, "An upper-limb rehabilitation exoskeleton system controlled by MI recognition model with deep emphasized informative features in a VR scene," *IEEE Transactions on Neural Systems and Rehabilitation Engineering*, 2023.
- [23] W. Li, Y. Ma, K. Shao, Z. Yi, W. Cao, M. Yin, T. Xu, and X. Wu, "The Human-Machine Interface Design Based on sEMG and Motor Imagery EEG for Lower Limb Exoskeleton Assistance System," *IEEE Transactions on Instrumentation and Measurement*, vol. 73, pp. 1–14, 2024.
- [24] L. Cheng, D. Li, G. Yu, Z. Zhang, and S. Yu, "Robotic arm control system based on brain-muscle mixed signals," *Biomedical Signal Processing and Control*, vol. 77, p. 103754, 2022.
- [25] J. Ai, J. Meng, X. Mai, and X. Zhu, "BCI control of a robotic arm based on SSVEP with moving stimuli for reach and grasp tasks," *IEEE Journal of Biomedical and Health Informatics*, 2023.
- [26] Y. Zhou, T. Yu, W. Gao, W. Huang, Z. Lu, Q. Huang, and Y. Li, "Shared three-dimensional robotic arm control based on asynchronous BCI and computer vision," *IEEE Transactions on Neural Systems and Rehabilitation Engineering*, 2023.
- [27] R. Fu, X. Feng, S. Wang, Y. Shi, C. Jia, and J. Zhao, "Control of the robotic arm system with an SSVEP-based BCI," *Measurement Science and Technology*, 2024.
- [28] L. Gu, Z. Yu, T. Ma, H. Wang, Z. Li, and H. Fan, "EEG-based classification of lower limb motor imagery with brain network analysis," *Neuroscience*, vol. 436, pp. 93–109, 2020.
- [29] H. Altaheri, G. Muhammad, M. Alsulaiman, S. U. Amin, G. A. Altuwaijri, W. Abdul, M. A. Bencherif, and M. Faisal, "Deep learning techniques for classification of electroencephalogram (EEG) motor imagery (MI) signals: A review," *Neural Computing and Applications*, vol. 35, no. 20, pp. 14 681–14 722, 2023.
- [30] J. Wang, L. Bi, and W. Fei, "EEG-Based Motor BCIs for Upper Limb Movement: Current Techniques and Future Insights," *IEEE Transactions on Neural Systems and Rehabilitation Engineering*, vol. 31, pp. 4413–4427, 2023.
- [31] Z. Liu, L. Wang, S. Xu, and K. Lu, "A multiwavelet-based sparse time-varying autoregressive modeling for motor imagery EEG classification," *Computers in biology and medicine*, vol. 155, p. 106196, 2023.

- [32] T. J. Bradberry, R. J. Gentili, and J. L. Contreras-Vidal, "Reconstructing three-dimensional hand movements from noninvasive electroencephalographic signals," *Journal of neuroscience*, vol. 30, no. 9, pp. 3432–3437, 2010.
- [33] A. Presacco, R. Goodman, L. Forrester, and J. L. Contreras-Vidal, "Neural decoding of treadmill walking from noninvasive electroencephalographic signals," *Journal of neurophysiology*, vol. 106, no. 4, pp. 1875–1887, 2011.
- [34] P. Ofner and G. R. Müller-Putz, "Decoding of velocities and positions of 3D arm movement from EEG," in *2012 annual international conference of the IEEE engineering in medicine and biology society*. IEEE, 2012, pp. 6406–6409.
- [35] A. Korik, R. Sosnik, N. Siddique, and D. Coyle, "Decoding imagined 3D hand movement trajectories from EEG: evidence to support the use of mu, beta, and low gamma oscillations," *Frontiers in neuroscience*, vol. 12, p. 323240, 2018.
- [36] Y. Sun, H. Zeng, A. Song, B. Xu, H. Li, J. Liu, and P. Wen, "Investigation of the phase feature of low-frequency electroencephalography signals for decoding hand movement parameters," in *2017 IEEE International Conference on Systems, Man, and Cybernetics (SMC)*, 2017, pp. 2312–2316.
- [37] R. Sosnik and O. B. Zur, "Reconstruction of hand, elbow and shoulder actual and imagined trajectories in 3D space using EEG slow cortical potentials," *Journal of neural engineering*, vol. 17, no. 1, p. 016065, 2020.
- [38] N. Robinson, T. W. J. Chester, and S. KG, "Use of Mobile EEG in Decoding Hand Movement Speed and Position," *IEEE Transactions on Human-Machine Systems*, vol. 51, no. 2, pp. 120–129, 2021.
- [39] F. Shakibae, E. Mottaghi, H. R. Kobravi, and M. Ghoshuni, "Decoding knee angle trajectory from electroencephalogram signal using NARX neural network and a new channel selection algorithm," *Biomedical Physics & Engineering Express*, vol. 5, no. 2, p. 025024, 2019.
- [40] J.-H. Jeong, K.-H. Shim, D.-J. Kim, and S.-W. Lee, "Brain-controlled robotic arm system based on multi-directional CNN-BiLSTM network using EEG signals," *IEEE Transactions on Neural Systems and Rehabilitation Engineering*, vol. 28, no. 5, pp. 1226–1238, 2020.
- [41] A. Jain and L. Kumar, "PreMovNet: Premovement EEG-Based Hand Kinematics Estimation for Grasp-and-Lift Task," *IEEE Sensors Letters*, vol. 6, no. 7, pp. 1–4, 2022.
- [42] S. Pancholi, A. Giri, A. Jain, L. Kumar, and S. Roy, "Source Aware Deep Learning Framework for Hand Kinematic Reconstruction Using EEG Signal," *IEEE Transactions on Cybernetics*, vol. 53, no. 7, pp. 4094–4106, 2023.
- [43] A. Jain and L. Kumar, "Subject-independent trajectory prediction using pre-movement EEG during grasp and lift task," *Biomedical Signal Processing and Control*, vol. 86, p. 105160, 2023.
- [44] M. Saini, A. Jain, S. P. Muthukrishnan, S. Bhasin, S. Roy, and L. Kumar, "BiCurNet: Premovement EEG-Based Neural Decoder for Biceps Curl Trajectory Estimation," *IEEE Transactions on Instrumentation and Measurement*, vol. 73, pp. 1–11, 2024.
- [45] B. J. Edelman, B. Baxter, and B. He, "EEG source imaging enhances the decoding of complex right-hand motor imagery tasks," *IEEE Transactions on Biomedical Engineering*, vol. 63, no. 1, pp. 4–14, 2015.
- [46] M.-A. Li, Y.-F. Wang, S.-M. Jia, Y.-J. Sun, and J.-F. Yang, "Decoding of motor imagery EEG based on brain source estimation," *Neurocomputing*, vol. 339, pp. 182–193, 2019.
- [47] Y. Hou, L. Zhou, S. Jia, and X. Lun, "A novel approach of decoding EEG four-class motor imagery tasks via scout ESI and CNN," *Journal of neural engineering*, vol. 17, no. 1, p. 016048, 2020.
- [48] V. S. Handiru, A. Vinod, and C. Guan, "EEG source space analysis of the supervised factor analytic approach for the classification of multi-directional arm movement," *Journal of neural engineering*, vol. 14, no. 4, p. 046008, 2017.
- [49] A. Tripathi, A. Gupta, A. Prathosh, S. P. Muthukrishnan, and L. Kumar, "NeuroAiR: Deep Learning Framework for Airwriting Recognition from Scalp-recorded Neural Signals," *IEEE Transactions on Instrumentation and Measurement*, pp. 1–1, 2024.
- [50] R. Sosnik and L. Zheng, "Reconstruction of hand, elbow and shoulder actual and imagined trajectories in 3D space using EEG current source dipoles," *Journal of neural engineering*, vol. 18, no. 5, p. 056011, 2021.
- [51] N. Srisrisawang and G. R. Müller-Putz, "Applying dimensionality reduction techniques in source-space electroencephalography via template and magnetic resonance imaging-derived head models to continuously decode hand trajectories," *Frontiers in human neuroscience*, vol. 16, p. 830221, 2022.
- [52] A. Jain and L. Kumar, "EEG Cortical Source Feature based Hand Kinematics Decoding using Residual CNN-LSTM Neural Network," in *2023 45th Annual International Conference of the IEEE Engineering in Medicine & Biology Society (EMBC)*, 2023, pp. 1–4.
- [53] M. D. Luciw, E. Jarocka, and B. B. Edin, "Multi-channel EEG recordings during 3,936 grasp and lift trials with varying weight and friction," *Scientific data*, vol. 1, no. 1, pp. 1–11, 2014.
- [54] A. Delorme and S. Makeig, "EEGLAB: an open source toolbox for analysis of single-trial EEG dynamics including independent component analysis," *Journal of neuroscience methods*, vol. 134, no. 1, pp. 9–21, 2004.
- [55] V. Fonov, A. C. Evans, K. Botteron, C. R. Almli, R. C. McKinstry, D. L. Collins, B. D. C. Group *et al.*, "Unbiased average age-appropriate atlases for pediatric studies," *Neuroimage*, vol. 54, no. 1, pp. 313–327, 2011.
- [56] A. Gramfort, T. Papadopoulos, E. Olivi, and M. Clerc, "OpenMEEG: opensource software for quasistatic bioelectromagnetics," *Biomedical engineering online*, vol. 9, no. 1, pp. 1–20, 2010.
- [57] F. Tadel, S. Baillet, J. C. Mosher, D. Pantazis, and R. M. Leahy, "Brainstorm: a user-friendly application for MEG/EEG analysis," *Computational intelligence and neuroscience*, vol. 2011, 2011.
- [58] R. D. Pascual-Marqui *et al.*, "Standardized low-resolution brain electromagnetic tomography (sLORETA): technical details," *Methods Find Exp Clin Pharmacol*, vol. 24, no. Suppl D, pp. 5–12, 2002.
- [59] A. Klein, B. Mensh, S. Ghosh, J. Tourville, and J. Hirsch, "Mindboggle: automated brain labeling with multiple atlases," *BMC medical imaging*, vol. 5, no. 1, pp. 1–14, 2005.
- [60] V. J. Lawhern, A. J. Solon, N. R. Waytowich, S. M. Gordon, C. P. Hung, and B. J. Lance, "EEGNet: a compact convolutional neural network for EEG-based brain-computer interfaces," *Journal of neural engineering*, vol. 15, no. 5, p. 056013, 2018.
- [61] R. T. Schirrmester, J. T. Springenberg, L. D. J. Fiederer, M. Glasstetter, K. Eggenberger, M. Tangermann, F. Hutter, W. Burgard, and T. Ball, "Deep learning with convolutional neural networks for EEG decoding and visualization," *Human brain mapping*, vol. 38, no. 11, pp. 5391–5420, 2017.